

<https://doi.org/10.1038/s43246-024-00714-x>

The role of redox and structure on grain growth in Mn-doped UO_2

Check for updates

Gabriel L. Murphy¹ , Elena Bazarkina^{2,3}, André Rossberg^{2,3}, Clara L. Silva^{2,3} , Lucia Amidani^{2,3}, Andrey Bukaemskiy¹, Robert Thümmeler¹, Martina Klinkenberg¹, Maximilian Henkes¹, Julien Marquardt⁴, Jessica Lessing², Volodymyr Svitlyk^{2,3}, Christoph Hennig^{2,3}, Kristina O. Kvashnina^{2,3} & Nina Huittinen^{2,5}

Mn-doped UO_2 is considered a potential advanced nuclear fuel due to ameliorated microstructural grain growth compared to non-doped variants. However, recent experimental investigations have highlighted limitations in grain growth apparently arising from misunderstandings of its redox-structural chemistry. To resolve this, we use synchrotron X-ray diffraction and spectroscopy measurements supported by ab initio calculations to cross-examine the redox and structural chemistry of Mn-doped UO_2 single crystal grains and ceramic specimens. Measurements reveal Mn enters the UO_2 matrix divalently as $(\text{Mn}_x^{+2}\text{U}_{1-x}^{+4})\text{O}_{2-x}$ with the additional formation of fluorite Mn^{+2}O in the bulk material. Extended X-ray absorption near edge structure measurements unveil that during sintering, the isostructural relationship between fluorite UO_2 and Mn^{+2}O results in inadvertent interaction and subsequent incorporation of diffusing U species within MnO, rather than neighbouring UO_2 grains, inhibiting grain growth. The investigation consequently highlights the significance of considering total redox-structural chemistry of main and minor phases in advanced ceramic material design.

The accelerated transition away from fossil fuels has highlighted limitations in current renewable energy infrastructure regarding security and intermittency. This has resulted in many nations examining nuclear energy to circumvent this by providing clean baseload power. In supporting this, additive doped- UO_2 nuclear fuels, involving the addition of typically small amounts of light elements such as Al and Cr during fuel fabrication^{1,2}, have drawn considerable attention by fuel vendors³ due to their improved in-reactor fuel efficiency and safety performance compared to traditional variants^{2,4}. In the gold standard case of Cr-doped UO_2 , the addition of Cr promotes enhanced grain growth of the fuel structure from a few microns in traditional non-doped pure UO_2 to 10–100 microns in the doped form^{5–8}. This enhanced grain growth leads to ameliorated fuel properties including increased density and improved thermal conductivity via reduced fission gas release^{2,9,10}. Although Cr-doped UO_2 fuels have endured sustained interest from industry and researchers alike due to their usage in power reactors, other dopants have also been considered including Ti, V, Fe, and Mn which all exhibit similar grain growth phenomena^{11–14}. Of these, Mn doped- UO_2 has been calculated^{11,12,15}, to display enhanced grain growth over Cr,

implying it possesses superior in-reactor fuel performance and can be considered for usage as an advanced nuclear fuel^{11,15}.

Experimental investigations of Mn-doped UO_2 which have examined potential improved grain growth from Mn doping have yielded mixed results. Zhong et al.¹⁶ using powder metallurgical preparation conditions was able to achieve a 2-fold increase in the average grain size of Mn-doped UO_2 compared to UO_2 with additional improvement of densification. In contrast, Smith et al.¹⁷ found only a marginal increase in the average grain size of Mn-doped UO_2 prepared using a nitrate precipitation method compared to UO_2 . More enhanced grain growth was obtained by Kang et al.¹⁸ in Mn-doped UO_2 who used additional Al_2O_3 as an eutectic mixture with MnO under powder metallurgical preparation conditions, leading to a 5-fold grain size increase in comparison to UO_2 . However, such increases still pale in comparison to Cr-doped UO_2 which can exhibit over a 20-fold increase in average grain size without requiring eutectic aids⁵, which is subsequently affront to simulation studies that argue for enhanced average size for Mn over Cr^{11,12,15}.

¹Institute of Fusion Energy & Nuclear Waste Management (IFN-2), Forschungszentrum Jülich GmbH, Jülich, Germany. ²Institute of Resource Ecology, Helmholtz-Zentrum Dresden-Rossendorf, Dresden, Germany. ³The Rossendorf Beamline at ESRF, The European Synchrotron, Grenoble, France. ⁴Institut für Geowissenschaften, Goethe-Universität Frankfurt, Frankfurt am Main, Germany. ⁵Institute of Chemistry and Biochemistry, Freie Universität Berlin, Berlin, Germany.

e-mail: g.murphy@fz-juelich.de

Ubiquitous and pertinent to Mn, Cr, and other fuel dopant additives is their ability to adopt a plethora of secondary phases including oxide, eutectic and metallic compositions associated with precipitates and grain boundaries in addition to concurrent lattice matrix incorporation^{5,7–9,19}. The origin of this behaviour is traced to the relatively small size of these dopants as cations compared to the large U^{+4} cation inhibiting lattice solubility coupled with the variable chemical behaviour during fuel sintering, which is dependent on exact applied temperature and oxygen potential (μ_{O_2})^{20,21}. Indeed, the equilibrium between the dissolved lattice matrix dopant metal cation chemistry and the occurrence of eutectic products during high-temperature sintering is understood to convey the enhanced grain growth phenomena via induced formation of the U vacancy defects, v_U'' , that become mobile and diffuse across the grain-boundary barrier contributing to growth and ultimately lead to improved properties as nuclear fuels^{8,22}. Concomitantly, this chemical complexity creates considerable challenges in experimentally determining specific dopant redox states, their chemistry and locality present even in fresh fuels reliably as bulk measurements inevitably contain convoluted signals arising from this myriad of chemical species present. Overcoming this challenge requires unique experimental approaches which can separate chemical environments and species that convolute measurements of target-specific regions of the fuel structure, such as the lattice, grain boundary regions and precipitates. It was recently demonstrated⁵ for Cr-doped UO_2 that this could be achieved via the extraction and measurement of representative single crystal grains from bulk material. This work identified in the bulk material that with concurrent lattice incorporated Cr^{+3} ($(Cr^{+3}_xU^{+4}_{1-x})O_{2-0.5x}$), secondary Cr phase Cr (Cr^0) and oxide related Cr^{+2} and $Cr^{+3}_2O_3$ were also present, consistent with the works of Riglet-Martial et al. and Leenaers et al.^{8,9}. In the case of Mn-doped UO_2 , depending on temperature and μ_{O_2} , metallic (Mn^0), $Mn^{+2}O$, $Mn^{+2+3}_3O_4$ and $Mn_2^{+3}O_3$ can be potentially accessed at fuel sintering conditions²¹, which may subsequently influence grain growth and the final ceramic material properties. Additionally, these phases allow for a variety of Mn redox options for UO_2 lattice incorporation. Subsequently, Mn-doped UO_2 can be considered a highly complex system, that is chemically distinct from Cr-doped UO_2 regarding dopant secondary phase chemistry and in which its total solid-state chemistry remains to be elucidated incontrovertibly. Beyond nuclear materials, establishing a complete phase assemblage in a material and gaining a global understanding of its solid-state chemistry is crucial. This pertinence is well established in fields like MAX compounds and lithium battery devices, where secondary phases can significantly affect the final usage and deployability of the materials^{23,24}. The same principle applies to Mn-doped UO_2 , which is being considered as a potential advanced nuclear fuel.

In the present investigation, mechanically extracted single crystal grains and bulk material of Mn-doped UO_2 , produced by sintering of pellets under conditions of 1700 °C (1973.15 K) and -420 kJ/mol synthesised with Mn additions of 500 ppm, 1000 ppm, and 2000 ppm, were examined using high energy resolution fluorescence detection X-ray absorption (HERFD-XANES) and extended X-ray absorption fine structure spectroscopy (EXAFS). By comparing spectroscopic results from the single crystal grains against the bulk material, specific Mn chemical states are identified and the redox state and mechanism of incorporation for Mn into UO_2 is determined. Possible other incorporation mechanisms into the UO_2 matrix were further explored by electronic structure calculations using ab initio simulations. Scanning electron microscopy (SEM) measurements were further used to understand the role of Mn doping to induce enhanced grain growth relative to pure UO_2 . The relationship between the lattice parameter of Mn doped- UO_2 with the amount of Mn added during synthesis is established via synchrotron X-ray powder diffraction (S-XRD) measurements on samples with 0 ppm, 500 ppm, 1000 ppm, and 2000 ppm and compared against recent results on the lattice parameter of Cr-doped UO_2 ²⁵, in order to compare relative lattice solubilities and chemistries under like synthesis conditions. By carefully inspecting the obtained results, the investigation highlights the significant role the chemistry of secondary phases has upon microstructural grain growth. In particular, the potential inadvertent

incorporation of ions that should contribute to main phase grain growth in secondary phases due to similar solid-state chemistries. The investigation is discussed in the context of doping effects on the microstructure of UO_2 in addition to the potential application of Mn-doped- UO_2 nuclear fuels for power generation regarding their chemical and microstructural properties.

Results and discussion

Synthesis and materials characterisation

Mn-doped UO_2 samples were synthesised based on an established method used previously for the synthesis of Cr-doped UO_2 involving precipitation and doping of ammonium diuranate (ADU)⁶ beginning with $UO_2(NO_3)_2$ and $Mn(NO_3)_2$. Additions of Mn for 0 ppm, 500 ppm, 1000 ppm, and 2000 ppm, as Mn elemental, in UO_2 were targeted for the synthesis of the samples with sintering conditions of 1700 °C (1973.15 K) and -420 kJ/mol. As described previously, the desirable enhanced grain growth in doped UO_2 fuels is understood to be primarily due to the occurrence of a eutectic, particularly a liquid phase during sintering temperature^{8,26}. MnO enters its liquid state at 1945 °C, however, such conditions are exceedingly higher than what is normally applied to UO_2 during fuel fabrication²⁶. In contrast, Mn and Mn_3O_4 enter their liquid states at lower temperatures of 1246 °C and 1567 °C, respectively. Accordingly, conditions of 1700 °C and -420 kJ/mol were chosen due to the relevance of fuel production, previous related studies on Cr-doped UO_2 ^{5,6} and favourability in inducing a partial liquid state (eutectic) for some Mn constituents at sintering conditions according to the Mn–O phase diagram²¹, thereby potentially allowing grain growth. S-XRD measurements analysed via the Rietveld method, indicated the formation of single-phase fluorite materials in space group $Fm\bar{3}m$ consistent with the general UO_2 fluorite structure for all examined compositions. Refinement profiles are given in Supplementary Information Note 1 and discussed in further detail in subsequent sections.

Electron microscopy microstructure analysis

Examination of the microstructures of a Mn doped- UO_2 pellet with 0 (pure UO_2) and 2000 ppm addition via SEM with energy dispersive X-ray spectroscopy (SEM-EDS), as shown in Fig. 1, indicated that the described synthesis conditions were successful in inducing enhanced grain growth in the Mn doped- UO_2 sample. Compared to a previous UO_2 standard generated under identical conditions⁵, the 2000 ppm Mn-doped UO_2 sample had a 2-fold increase in average grain size to 11.6 μm , consistent with previous work by Zhong et al.¹⁶, further details are provided in Table 1. However, compared to Cr-doped UO_2 , such a grain enlargement in Mn-doped UO_2 is considerably lower, whereas for samples prepared under like conditions but slightly higher Cr addition at 2395 ppm there is a 20-fold increase⁵. Additionally, SEM measurements were made against the 500 ppm and 1000 ppm Mn addition samples where a subtle but gradual trend of increasing grain size with increased Mn addition could be observed. These results are provided in Supplementary Information Note 2. Interestingly, EDS measurements could not resolve enriched Mn states in the bulk structure of Mn-doped UO_2 noting the resolution limit of 0.1 wt.% as evident in Fig. 1d. Such enriched regions are readily observable in Cr-doped UO_2 ^{5,7,9} in the form of metallic and oxide Cr for samples prepared under like conditions. This lack of observable Mn from SEM-EDS is likely attributed to either the loss of Mn through volatilisation, which the conditions used to synthesise Mn-doped UO_2 are conducive to^{27,28}, or extensive incorporation into the UO_2 structure which when homogeneously incorporated would not be detectable considering doping levels used in synthesis. Additionally, from SEM-EDS analysis no evidence for a eutectic phase could be observed.

From the SEM analysis of the Mn-doped UO_2 sample with a 2000 ppm addition of Mn, it was determined that single crystal grains would be of appropriate size for mechanical extraction and subsequent analysis. The extraction of the single crystal grains was achieved by direct mechanical separation from the bulk ceramic material (described in the “Methods”) as performed previously in our studies of Cr-doped UO_2 ⁵. The directness of the approach, i.e. not relying on other synthesis methods or techniques for single crystal acquisition, meant the crystals were completely representative

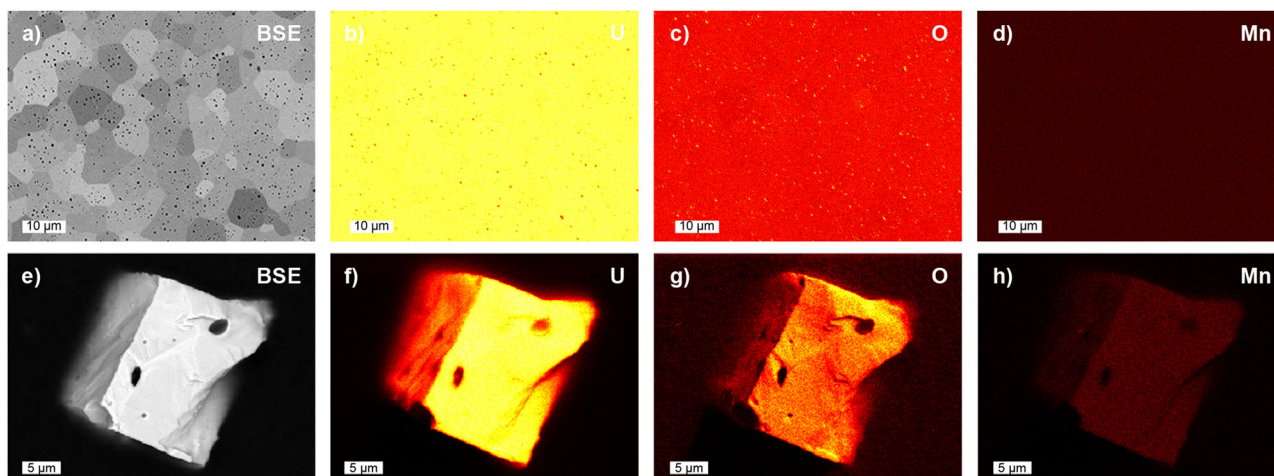


Fig. 1 | Electron micrographs of bulk Mn-doped UO_2 and a single crystal extracted from the parent material. BSE (a, e) and EDS (b–d, f–h) U L-, O K- and Mn K-edge images of Mn-doped UO_2 pellets (top) with 2000 ppm addition as Mn shown comparatively with a single crystal grain (bottom) extracted from the same

material. Note the lack of impurity grains and excess Mn additions on the surface of the single crystal grain, particularly in void regions, compared to the pellet. The dark spots in the single crystal grain BSE are due to voids and note the shadow effect from EDS present in the U L-, O K- and Mn K-edges.

of the bulk material. SC-XRD measurements confirmed the single-crystal nature of the specimens and further analysis confirmed they were UO_2 fluorite structured in space group $Fm\bar{3}m$. SC-XRD analysis results for a variety of extracted crystals are provided in Supplementary Information Note 3. No parasitic, near-surface Mn-associated impurities were identified (Fig. 1) from SEM-EDS measurements and potential sub-surface impurities were not supported by further HERFD-XANES spectroscopic measurements, discussed in later sections. The morphological and impurity contrast between the single crystal grains and bulk material is illustrated in Fig. 1.

HERFD-XANES spectroscopy—spectroscopic analysis

HERFD-XANES measurements of Mn-doped UO_2 bulk material with 2000 ppm addition of Mn and an extracted single crystal grain were measured on the Mn K-edge with metallic Mn (Mn^0), $\text{Mn}^{+2}\text{Cl}_2\cdot 4\text{H}_2\text{O}$, Mn^{+3}F_3 , Mn^{+2}O , Mn^{+3}O_3 , and Mn^{+4}O_2 standards. From observing the normalised HERFD-XANES spectra, it was determined that both the Mn-doped UO_2 bulk material and an extracted single crystal grain contained only divalent Mn species. Accordingly, Fig. 2, provides the normalised HERFD-XANES spectra for the Mn-doped UO_2 bulk material and extracted single crystal grain with the measured standards $\text{Mn}^{+2}\text{Cl}_2\cdot 4\text{H}_2\text{O}$ and Mn^{+2}O induced. The HERFD-XANES spectra of the Mn-doped UO_2 bulk material and extracted single crystal grain with all measured standards overlaid can be viewed in Supplementary Information Note 4.

Inspecting Fig. 2, the normalised HERFD-XANES Mn K-edge spectra of the bulk Mn-doped UO_2 powder with 2000 ppm Mn were found to contain spectral signatures closely resembling the $\text{Mn}^{+2}\text{Cl}_2\cdot 4\text{H}_2\text{O}$, and particularly Mn^{+2}O standards. In contrast, the spectra of the Mn-doped UO_2 single crystal grain have features more consistent with the white line/main edge position of the $\text{Mn}^{+2}\text{Cl}_2\cdot 4\text{H}_2\text{O}$ standard. The contrast of the

HERFD-XANES spectra of the crystal against the bulk is particularly evident by the broad post-edge oscillation at approximately 6562 eV in the Mn doped- UO_2 single crystal spectrum. The variation in the smoothness of the single crystal grain spectrum is associated with the presumed low amount of Mn with the single crystal grain coupled with its size. In contrast to the spectrum of the single crystal grain, a broad post-edge oscillation at 6568 eV matching well with the features of the Mn^{+2}O standard is observed in the Mn doped- UO_2 powder. Further differences can be observed at the main edge between the two specimens. This difference in HERFD-XANES spectra between the bulk and single crystal, is understood to be a consequence of the variable Mn chemical states, particularly Mn^{+2}O , which is present in the former, but absent in the latter. Pertinently, for both sample types only Mn^{+2} is present in the materials, and there is no evidence for other redox states of Mn present in Mn-doped UO_2 (see Supplementary Information Note 4). Nevertheless, the bulk material is inevitably richer in chemical states than the single crystal and it appears to contain non-lattice associated Mn^{+2}O , which is attributed to a secondary phase species, associated with either grain boundary regions or present as trace or nano-sized precipitates, as EDS measurements were unable to resolve Mn-enriched clusters. Considering the combined observations from HERFD-XANES and EDS measurements, the amount of Mn in the bulk material must be extremely low, and likely affected by volatilisation consistent with previous studies^{13,21,27,28}. Invariably, HERFD-XANES measurements of the single crystal grains show an absence of MnO, indicating the observed signal is arising from the purely UO_2 lattice incorporated Mn^{+2} .

To probe the changes to the U redox during the incorporation of Mn^{+2} into the UO_2 , HERFD-XANES measurements were performed on the U M_4 -edge and U L_3 -edge for the Mn-doped UO_2 bulk powder with 2000 ppm of Mn and U L_3 -edge for the single crystal grain extracted therefrom. These results, provided in Fig. 3, show that both the single crystal grain and bulk material contain U^{+4} . Critically, the incorporation of Mn into the UO_2 occurs at a trace level, in which changes to the U oxidation state are not expected to be distinguishable at such low incorporated levels from HERFD-XANES U M/L-edge measurements, for instance, the occurrence of U^{+5} . Nevertheless, the U M_4 -edge and U L_3 -edge do show that the examined materials are near stoichiometric as targeted from applied sintering conditions.

HERFD-XANES spectroscopy—electronic structural modelling

From the HERFD-XANES experimental analysis, it was demonstrated that Mn was incorporated into the UO_2 matrix as Mn^{+2} with the additional formation of Mn^{+2}O in the bulk material. What is not clear is the exact

Table 1 | Minimum, maximum, mean grain sizes, and number of analysed grains of the UO_2 pellets doped with reference 0 ppm and 2000 ppm Mn in addition to Cr-doped UO_2 with 2395 ppm Cr as addition⁵

	0 ppm ⁵	Mn 2000 ppm	Cr 2395 ppm ⁵
Minimum, [μm]	0.4	0.4	4.9
Maximum, [μm]	41.7	41.7	290.1
Mean, [μm]	5.0	11.6	103.4
Number of grains	1745	858	401

Note that grain size determination carries an uncertainty of ± 0.8 μm.

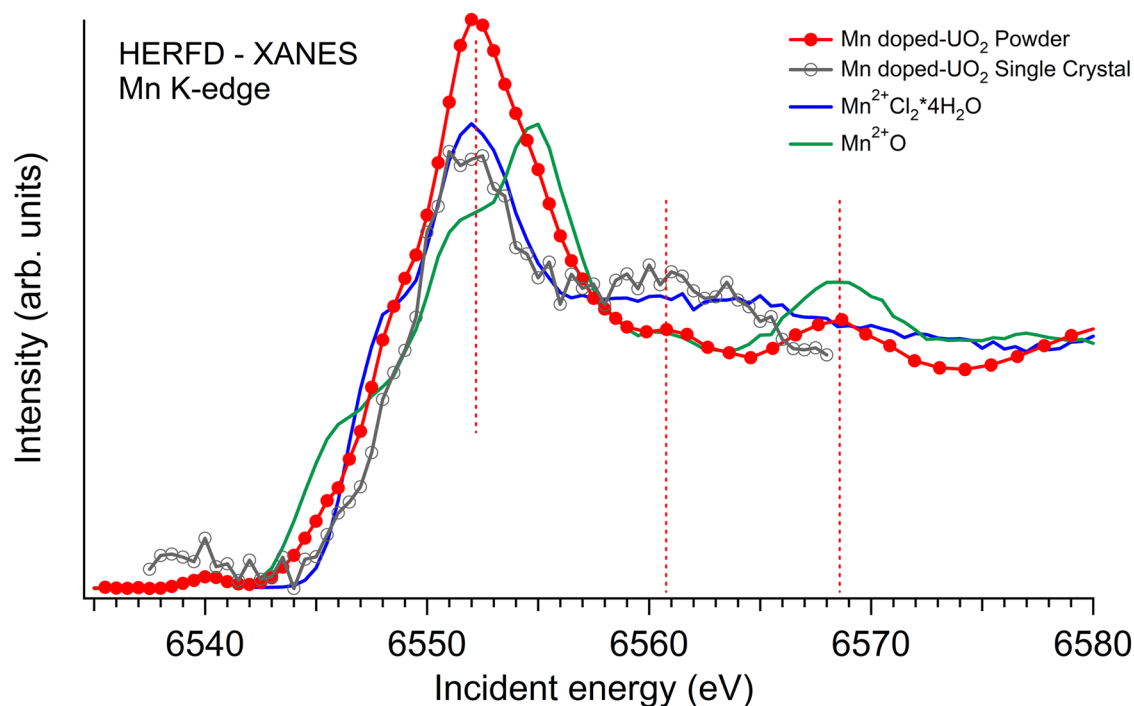


Fig. 2 | Mn K-edge HERFD-XANES spectroscopic analysis of the Mn-doped UO₂ single crystal grain and bulk material with select standards. Normalised Mn K-edge HERFD-XANES spectra in the range 6540 eV to 6580 eV for Mn-doped UO₂

as bulk powder and single crystal grain with measured standards Mn²⁺Cl₂·4H₂O, and Mn²⁺O. Vertical dashed red lines are used to indicate differences between the Mn-doped UO₂ single crystal and bulk powder.

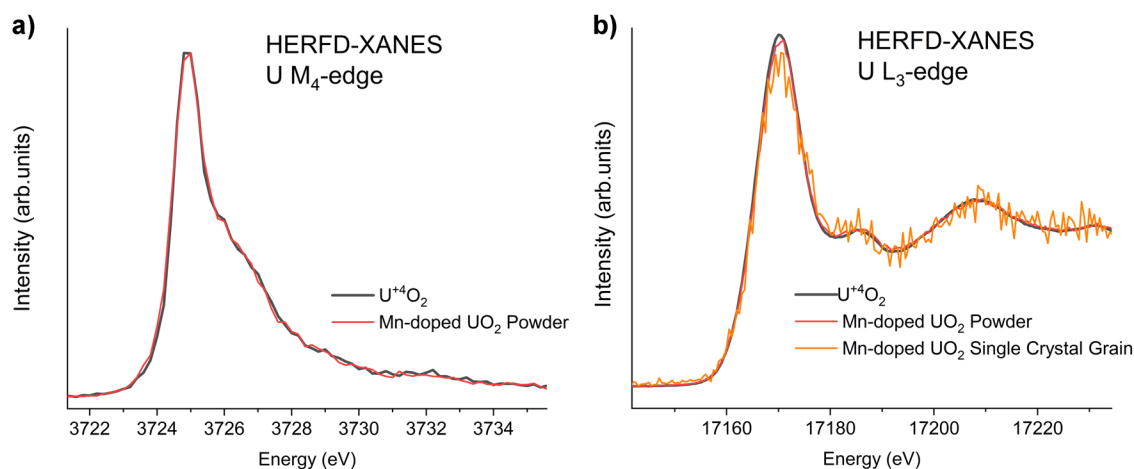


Fig. 3 | U M₄- and L₃-edge HERFD-XANES spectroscopic analysis of the Mn-doped UO₂ single crystal grain and bulk material with U⁴⁺ standard.

a Normalised U M₄-edge HERFD XANES spectra for UO₂ and Mn-doped UO₂ powder with 2000 ppm addition as Mn and **b** Normalised U L₃-edge HERFD XANES spectra for UO₂, Mn-doped UO₂ powder with 2000 ppm addition as Mn

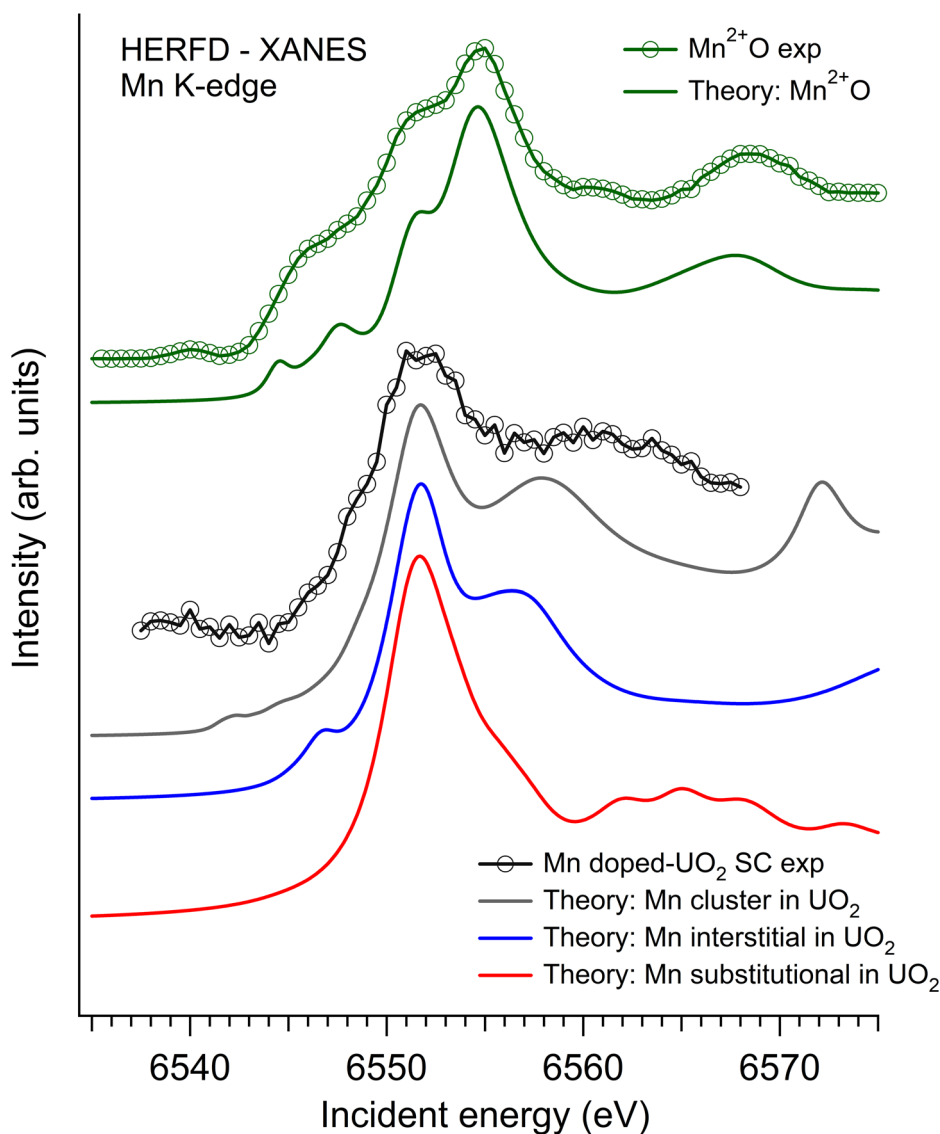
and a single crystal grain. The consistent line shape and position between the Mn-doped UO₂ powder and the single crystal grain spectrum with UO₂ indicates the absence of U⁵⁺ and the sole presence of U⁴⁺. The increased noise in the single crystal grain line spectrum is due to its small relative size.

structural mechanism for incorporation such as interstitial or substitutional. Although the single crystal grain HERFD-XANES spectra provide a definitive conclusion for the redox state of Mn within UO₂ as +2, the considerable noise in the signal at the post-edge region arising from the low amount of measurable Mn in the small single crystal grain makes it difficult to draw definitive conclusions on regarding exact incorporation mechanism based on measurement alone. In order to shed further light on the incorporation mechanism electronic structure calculations were performed using the finite difference method near-edge structure (FDMNES)²⁹ code in which the Mn K-edge was calculated considering three structural models. Mn incorporation in the UO₂ structure was considered as a cluster, as an

interstitial atom, and in a substitutional position. The results of these calculations are provided in Fig. 4.

Evident from Fig. 4, the HERFD-XANES K-edge spectra of the Mn-doped UO₂ single crystal grain can be best reproduced when one isolated Mn²⁺ cation is included in the structure substituting for a U⁴⁺ position. Other options, such as the occurrence of clusters or an interstitial can be largely ruled out. In the case of the interstitial mechanism, the distinct pre-edge feature is not present in the single crystal grains spectrum. Similarly, both pre- and post-edge features in the cluster mechanism are also not present in the single crystal grain's spectrum. Although the low HERFD-XANES intensity of the single crystal grain prevents an unequivocal

Fig. 4 | Ab initio calculations of Mn K-edge HERFD-XANES spectra arising from different substitution models of Mn in UO₂ compared to measurement. HERFD-XANES Mn K-edge spectra collected for the Mn²⁺O reference and Mn-doped UO₂ single crystal compared with simulations obtained by FDMNES. Three structural models were considered for the Mn incorporation in UO₂: Mn as a cluster, Mn as an interstitial atom, and Mn in a substitutional position.



conclusion, to the limits of measurement and comparison to the theoretical modelling the incorporation of Mn²⁺ into the UO₂ lattice can be described as occurring through a substitutional mechanism for U⁴⁺. Such a mechanism was argued also by Smith et al.¹⁷ based on their EXAFS analysis of the bulk material. A similar conclusion is made in the present manuscript described subsequently also by EXAFS. It is further noteworthy that Cooper et al.¹² described the lattice substitutional mechanism of Mn into UO₂ as dominant below 1400 K.

Synchrotron X-ray powder diffraction

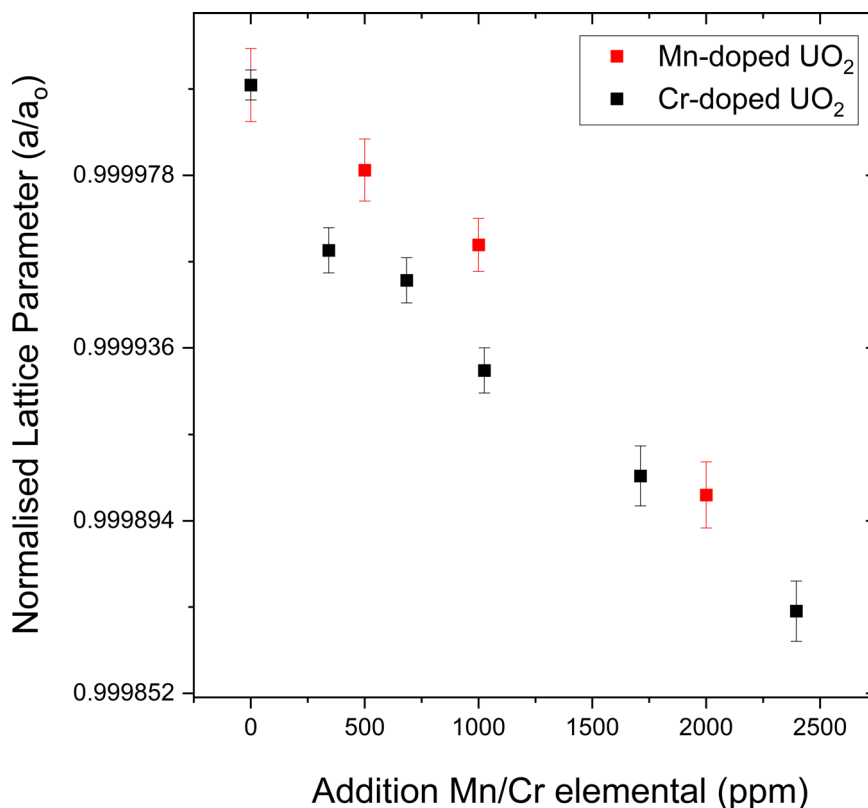
The incorporation of the vastly smaller Mn²⁺ cation into the UO₂ lattice via the described mechanisms will induce a lattice contraction, similar to that observed in Cr-doped UO₂²⁵. The contraction inevitably depends on the amount of Mn²⁺ that enters the fluorite crystal lattice which observations from this study so far, indicate the amount is quite low, consistent with literature¹⁷. To precisely understand the relationship between the lattice dependence of Mn²⁺ incorporation into UO₂, high-resolution measurements are necessary in the form of S-XRD measurements. S-XRD measurements were performed against Mn-doped UO₂ powder samples involving 0 ppm, 500 ppm, 1000 ppm, and 2000 ppm of Mn additions. Observation of collected diffractograms showed very subtle shifting of Bragg reflections as illustrated in Supplementary Information Fig. 1. The collected diffraction patterns were analysed using the Rietveld method to precisely

determine associated lattice parameters and their contraction from doping. In Fig. 5 the normalised lattice parameter (a/a_0) is plotted as a function of Mn addition with recent results from Cr-doped UO₂ also determined from S-XRD measurements and synthesised using identical conditions²⁵. Determined lattice parameter values are provided in Table 2 and Rietveld refinement profiles for all measured compositions in Supplementary Information Fig. 1.

As can be observed from Fig. 5, the doping of Mn into UO₂ under synthesis conditions of 1700 °C and −420 kJ/mol involves only very minor contraction of the fluorite lattice, which is largely comparable to Cr-doped UO₂ prepared under like synthesis conditions⁵. Such conditions are established for Cr-doped UO₂ to result in a solubility limit of 750 ppm of Cr⁸. Structurally, the addition of Cr³⁺ into the UO₂ lattice matrix should induce a larger contraction of the lattice parameter compared to Mn²⁺ owing to its smaller ionic radii (0.615 Å vs 0.67 Å, respectively³⁰). Inspection of Fig. 5 shows that this appears to be consistent but also relatively comparable when comparing additions of Mn vs Cr with associated determined lattice parameters. This subsequently suggests that the solubility of Mn in UO₂ is similar to Cr. This argument is consistent with the work of Kleykamp³¹ who examined the reaction of UO₂ with steel, finding relatively similar incorporation rates and amounts of Cr and Mn in UO₂.

The incorporation of either Cr³⁺ or Mn²⁺ into UO₂ requires a charge balancing mechanism occurring through either the formation of oxygen

Fig. 5 | Synchrotron X-ray powder diffraction analysis of Mn-doped UO_2 with different Mn additions compared to Cr additions under like synthesis conditions. Normalised lattice parameters, a/a_0 , of Mn-doped UO_2 with 0 ppm, 500 ppm, 1000 ppm, and 2000 ppm addition of Mn elemental determined from Rietveld refinements against S-XRD data plotted comparatively with Cr-doped UO_2 ⁵ prepared under like conditions of 1700 °C and -420 kJ/mol and also measured using S-XRD.



vacancies, $v_o^{\bullet}/v_o^{\bullet\bullet}$, or oxidised uranium, U^{+5} . It has been shown that the formation of $v_o^{\bullet}/v_o^{\bullet\bullet}$, which is inherently larger than O^{-2} in UO_2 due to Coulombic repulsion from the nearest neighbours, will result in a local lattice expansion³². In contrast, the formation of U^{+5} will result in additional lattice contraction with the inclusion of Cr^{+3} or Mn^{+2} cations, as U^{+5} is smaller than U^{+4} ³⁰. In this case of aliovalent substitution of larger cations with relatively smaller cations, it is generally accepted that this occurs via oxygen defects rather than host cationic lattice oxidation as this will minimise total lattice strain. Such behaviour has been previously described in studies of UO_2 for both small and large cation substitution³² and is consistent with what was observed in Cr-doped UO_2 ⁵. Furthermore, the subsequent corresponding rate of lattice contraction will be naturally dependent upon which mechanism is followed. For example, U^{+5} formation result in a greater degree of lattice contraction than would with oxygen defect formation for the corresponding amount of dopant. Considering the observed trends in Fig. 5, particularly the very similar rate of lattice contraction between Cr-doped UO_2 and Mn-doped UO_2 , it strongly suggests that the mechanism of incorporation of Mn into UO_2 is similar and subsequently follows an oxygen defect mechanism. Consequently, considering the HERFD-XANES results and associated simulations, the substitution mechanism can be described as $(\text{Mn}_x^{+2}\text{U}_{1-x}^{+4})\text{O}_{2-x}$.

Table 2 | Refined structural parameters for Mn-doped UO_2 with 0 ppm, 500 ppm, 1000 ppm, and 2000 ppm Mn addition determined from S-XRD data with $\lambda = 0.7749$ Å

Mn addition ppm	Lattice parameter, (Å)	wRp, (%)	Rp, (%)
0	5.47060(5)	6.66	5.23
500	5.47049(4)	6.53	5.08
1000	5.47039(4)	5.34	4.35
2000	5.47005(4)	8.55	6.1

The structures were refined in a cubic fluorite structure with space group $Fm\bar{3}m$.

EXAFS spectroscopy

Given the results so far of the investigation, it is surprising that despite apparent similar levels of solubility of Mn to Cr as indicated by S-XRD measurements, the degree of grain growth is considerably lower in Mn-doped UO_2 compared to Cr-doped UO_2 even when accounting for variable volatility^{26–28} and considering previous predictions¹². Cr-doped UO_2 can often form a eutectic composition²² that aids grain growth, but this was not observed in the present investigation for Mn-doped UO_2 . Mn-doped UO_2 has been previously synthesised with a eutectic through Al_2O_3 addition by Kang et al.¹⁸, which did improve grain growth, but still not to the same extent as achieved in Cr-doped UO_2 ⁵. A reason behind the limited grain growth can be related to insufficient defect formation and transport across the grain boundary region³³. The grain growth of UO_2 via doping with Mn, Cr and other transition metals is understood to be assisted by both eutectic formation in addition to lattice matrix vacancy defect¹². In particular uranium-based vacancies, $v_U^{\bullet\bullet}$, that are mobile at sintering conditions and allow grain growth to occur ultimately. In an attempt to try to understand the microstructural-chemical processes that may be occurring and affecting the microstructure of Mn-doped UO_2 , EXAFS measurements on the Mn K-edge were performed on bulk Mn-doped UO_2 with 2000 ppm addition of Mn. Considering the results of the HERFD-XANES, that Mn^{+2} exists in two chemical environments, respectively as Mn^{+2} -doped UO_2 lattice matrix and Mn^{+2}O , the EXAFS fitting was performed assuming two environments. This required splitting the first Mn–O shell into two individual Mn–O shells. The validity of the shell splitting was tested against fits using a single Mn–O shell. The results of both fits are compiled in Supplementary Information Note 5. In the single shell fit, the Mn–O shell at 2.22 Å shows a large Debye–Waller factor (σ^2) of 0.023 Å², which points toward the presence of different chemical surroundings for Mn with different first shell Mn–O distances. Note that for a structurally ordered pure MnO phase with six coordinating oxygen atoms at a similar distance, a much smaller σ^2 would be expected. Another justification for including two first Mn–O shells, is the very low coordination number of 3 instead of 12 for the Mn–Mn shell at 3.10 Å, pointing toward the presence of structurally different Mn

Table 3 | EXAFS fit parameters for Mn K-edge data measured from Mn-doped UO₂ powder with the addition of 2000 ppm Mn with reference structural parameters from UO₂ and MnO

Path	CN	R/Å	$\sigma^2/\text{Å}^2$	dE0/eV
First shell Mn–O interaction split into two shells				
Mn–O	3.0(8)	2.14(2)	0.009(8)	8.95(9)
Mn–O	3.0+	2.32(3)	0.009/	8.95/
Mn–Mn	3(1)	3.100(7)	0.002(4)	8.95/
Mn–O	4(1)	3.73(6)	0.008f	8.95/
Mn–Mn	5.7(8)	4.10(1)	0.008f	8.95/
Mn–O	5(3)	4.97(7)	0.008f	8.95/
Mn–Mn	15(2)	5.45(1)	0.008f	8.95/
Mn–U	13(4)	5.70(2)	0.008f	8.95/
Mn–U	12(4)	6.00(3)	0.008f	8.95/
Mn–Mn	21(4)	7.05(2)	0.008f	8.95/
Mn–U	18(4)	7.34(2)	0.008f	8.95/
UO₂ powder: Degranges et al.⁵⁰				
U–O	–	2.3677(5)	–	–
U–U	–	3.8665(8)	–	–
U–O	–	4.59(2)	–	–
U–O	–	4.5338(9)	–	–
U–U	–	5.4680(11)	–	–
U–O	–	5.9586(11)	–	–
U–U	–	6.6969(13)	–	–
U–O	–	7.1031(14)	–	–
U–U	–	7.7329(15)	–	–
MnO powder: Sasaki et al.³⁴				
Mn–O	–	2.2230(6)	–	–
Mn–Mn	–	3.1438(8)	–	–
Mn–O	–	3.8503 (9)	–	–
Mn–Mn	–	4.4460(11)	–	–
Mn–O	–	4.9708(12)	–	–
Mn–Mn	–	5.4452(13)	–	–
Mn–O	–	6.6690(16)	–	–
Mn–Mn	–	6.2876(15)	–	–
Mn–O	–	7.3729(17)	–	–
Mn–Mn	–	7.0297(16)	–	–

CN coordination number, *R* radial distance, σ^2 squared Debye–Waller factor, *dE0* shift in energy threshold, *f* fixed parameter, / linked parameter, + constant sum. Estimated standard deviations of the variable parameter as calculated by EXAFSPAK⁴⁶.

CIFs provided by Degranges et al.⁵⁰ using neutron diffraction and Sasaki et al.³⁴ using X-ray diffraction. For the Mn-doped UO₂ EXAFS, the first Mn–O shell is split to reflect the two different Mn environments in the sample.

phases in the samples. Thereby, the splitting of the Mn–O shell is justified, although the two resulting Mn–O distances for this shell are close to the resolution limit of 0.22 Å for the radial distances, due to the available *k*-range. The corresponding fitting results are compiled in Table 3. The final analysed Mn K-edge spectrum of Mn-doped UO₂ (black) with corresponding FT and shell fit with residual between shell fit and the experimental spectrum is provided in Fig. 6. Additionally, both fit assuming with and without the first Mn–O shell split are provided in Supplementary Information Note 5.

Inspecting the determined structural parameters from Table 3 the first shell Mn–O distance when split was found to be 2.14(2) Å and 2.32(3) Å. Neither of the distances is overly close with the M–O length (*M* = Mn or U) of 2.223 Å and 2.368 Å in the pristine MnO or UO₂ structures, respectively.

While the 2.32 Å Mn–O bond length is rather similar to the U–O bond in UO₂, Mn incorporation into the UO₂ structure would be expected to cause a larger contraction of the distances to coordinating oxygens. Especially in light of previous results obtained for incorporated Cr⁺³ in the UO₂ lattice matrix, for which a Cr–O bond length of 1.94 Å was observed⁵. Thereby, the Mn–O bond distance of 2.14(2) Å is assigned to the lattice matrix incorporated Mn⁺². This supports the HERFD-XANES analysis that the Mn⁺² directly substitutes onto the U⁺⁴ position and involves a substitutional rather than interstitial mechanism. The 2nd Mn–O bond length of 2.32(3) Å is clearly longer than the average Mn–O bond length of 2.22 Å in the crystallographic MnO structure³⁴. It is strikingly similar to the standard U–O bond length of 2.3677(5) Å in UO₂, however, the small Mn⁺² cation should not induce such a small bond contraction when comparing the sizes of the Mn⁺² and U⁺⁴ as previously discussed. Instead, a bond-elongation compared to the MnO structure can be explained if assuming U-incorporation into the MnO structure, thereby causing an expansion of the average Mn–O distances from their crystallographic values.

Further indications for multiple phases in the powder sample can be obtained from the metal-metal scattering shells. The scattering shells at $R + \Delta r > 3.1$ Å can only be explained when considering both Mn–Mn and Mn–U scatterers in addition to Mn–O. Two Mn–U distances are found at 5.70(2) Å and 6.00(3) Å, indicative of two similar but not identical phases in the sample. Such observations were not previously made in Cr-doped UO₂⁵. In examining the Mn–U distances, the shorter distance of 5.70(2) Å is too long for the corresponding U–U distance in UO₂ of 5.4680(1) to account for a Mn⁺² substitution in UO₂, since it should induce a contraction, and is further far too short for the next U–U distance of 6.6969(13) Å. Substitution of the U⁺⁴ cation into the MnO structure would induce a bond expansion due to the larger U⁺⁴ cation compared to Mn⁺² and inspecting the Mn–Mn distances for MnO, the Mn–Mn distance of 5.4452(13) Å would be plausible for this considering there is a difference of ~0.3 Å between the determined Mn–U distance of 5.70(3) Å and this one, in addition to the approximate 0.33 Å difference in size of the Mn⁺² and U⁺⁴ cation. Similarly, such a substitution would induce an Mn–O bond elongation as is apparently observed in the first shell that is determined to be 2.32(2) Å compared to that encountered in MnO of 2.2230(6) Å. The 2nd determined Mn–U distance of 6.00(3) Å accordingly fits closer to the U–U distance of 6.6969(13) Å in UO₂ and likely reflects the Mn⁺² cation within the UO₂ structure since it would induce a bond contraction. The magnitude of the bond contraction (approximately 10%) is similar to the first shell Mn–O contraction discussed above. A similar behaviour, where the distortions to the UO₂ crystal lattice upon the incorporation of the smaller additive cation are not dampened for the second (or higher) coordination shells, has also been established for Cr⁺³ in UO₂, corroborating the assignment of these scattering shells to lattice matrix incorporated Mn⁺².

Moreover, the EXAFS analysis strongly indicates that there are not only two different Mn⁺² environments present within the bulk Mn-doped UO₂ material, consistent with the HERFD-XANES analysis, but there appear to be two different U environments. Subsequently, this suggests that during material sintering, in addition to Mn⁺² incorporating into UO₂, there appear to be U cations becoming incorporated within the MnO secondary phase. It is established that during material sintering and grain growth, it is required that $v_U^{''''}$ are able to diffuse across the grain boundary to other UO₂ grains allowing their growth and promoting further ion transport. Critically, MnO possesses a fluorite structure in space group *Fm* $\bar{3}$ *m* isostructural to UO₂, in which although there is a considerable size difference in the structures host cations, the isostructural relationship would allow for some mutual cation incorporation, specifically U cations entering the MnO structure instead of intended UO₂ grains via solid solution. Such behaviour would not be expected to be present within Cr-doped UO₂ since none of the Cr secondary phases, Cr₂O₃, Cr₃O₄, Cr⁰ etc. possess isostructural fluorite oxide structures in space group *Fm* $\bar{3}$ *m*, hence U incorporation would be relatively unfavourable. It is subsequently suspected that the poor observed grain growth in Mn-doped UO₂, contrary to theoretical predictions¹², may originate from U cations becoming inadvertently incorporated into secondary phase MnO,

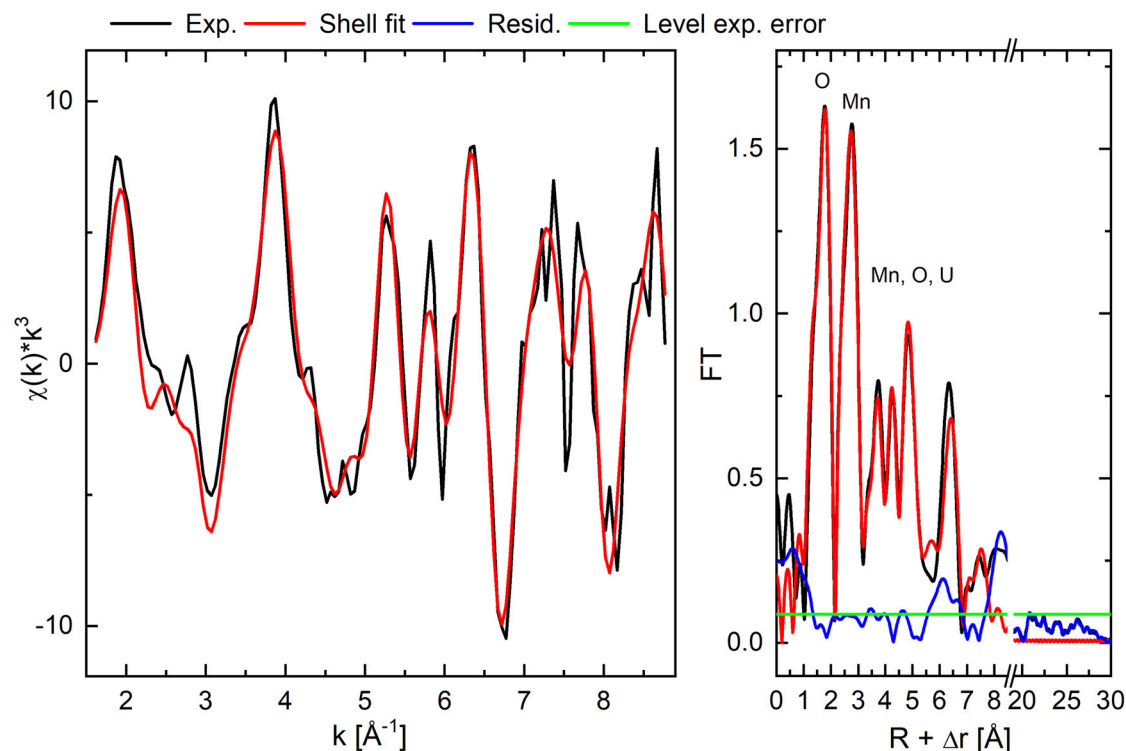


Fig. 6 | EXAFS analysis of Mn-doped UO_2 bulk material. Mn K-edge spectrum of Mn-doped UO_2 (black) with corresponding FT (right) and shell fit (red). The residual (resid.) between shell fit and experimental (exp.) data is given in blue. The level of

experimental error (green) is estimated by using the maximum FT amplitude in the R-range 20–30 Å. For the present analysis, the first shell of the Mn–O interaction is split into two shells reflecting the dual environments of Mn present in the samples.

rather than intended UO_2 , inhibiting growth during sintering of these materials at high temperatures.

Redox and bulk structural chemistry in Mn-doped UO_2

By extracting single crystal grains from bulk material and cross-analysing using X-ray diffraction and absorption spectroscopy under ambient conditions supported by theoretical ab initio calculations it was determined that in bulk Mn-doped UO_2 , the Mn cation enters the UO_2 lattice matrix substitutionally where it occurs divalently as $(\text{Mn}_x^{+2}\text{U}_{1-x}^{+4})\text{O}_{2-x}$ with the occurrence of secondary phase Mn^{+2}O . It was further found from SEM-EDS analysis, consistent with previous results^{16–18}, that the addition of Mn into UO_2 results in only moderate grain growth, inferior to that obtained from Cr doping⁵, despite apparent similar levels of lattice solubility as shown from S-XRD measurements compared to Cr doping²⁵ which also follows a similar incorporation mechanism, $(\text{Cr}_x^{+3}\text{U}_{1-x}^{+4})\text{O}_{2-0.5x}$ ⁵. These results are naturally contrary to previous theoretical calculations^{11,12}. This disparity can be crucially understood when considering the results of the EXAFS which show that in addition to Mn incorporation within UO_2 during sintering at 1700 °C U cations are also apparently becoming incorporated within the MnO secondary phase. It is subsequently argued that the isostructural relationship that exists between UO_2 and MnO likely facilitates this process occurring, however, this is at the detriment of the grain growth of UO_2 , since cations that should migrate to other UO_2 grains during sintering are lost to the MnO secondary phase via solid solution. Since MnO was not detected from the HERFD-XANES measurements in the single crystal grains, it strongly indicates the origin of MnO in the bulk material arises from either precipitates that are not detectable with SEM-EDS or more likely found within grain-boundary regions. Although not performed in this study, works by Zhong et al. have highlighted the enrichment of MnO along the grain boundary in highly Mn-doped UO_2 via electron microscopy measurements³⁵ whereas similar observations have also been made for Cr doping¹⁹. Hence their occurrence in these regions interrupts and detriments grain growth during sintering. This process is graphically summarised in Fig. 7.

The identification of parasitic but also volatile MnO occurring along with main phase UO_2 in Mn-doped UO_2 is significant when considering previous studies¹⁵, particularly modelling-based^{11,12,15}, which were performed without this knowledge. These, and related studies involving the chemistry and particularly grain growth of Mn-doped UO_2 would be subsequently impacted without having this complete materials chemistry accounted for. This process of inadvertent cation incorporation into secondary phases during material sintering consequently has significant implications for the design of large grain ceramics for nuclear and advanced material applications amongst others, in which it points towards the pertinence of considering the total chemistry of a ceramic system. The apparent critical effect a secondary phase can have upon bulk material performance is reminiscent of $\alpha\text{-Al}_2\text{O}_3$ formation on MAX phases, which leads to their stabilisation³⁶, or the occurrence of oxygen-deficient Li spinel structures within $\text{LiMn}_{0.05}\text{Mn}_{1.95}\text{O}_4$ battery materials that detrimentally effects their performance²⁴. In the case of UO_2 , many other dopants can be considered for usage in enhancing grain growth and have been done so. For instance, good results have been observed for Ti, Nb, and naturally Cr³⁷, yet when one considers their thermodynamic phase diagrams and potential structures under fuel sintering conditions, they are not conducive to fluorite-type oxide/dioxide occurrence like Mn is, which as this investigation points to, may inhibit grain growth via unfavourable solid solution behaviour.

Conclusion

Mn-doped UO_2 ceramics with Mn additions of 0 ppm, 500 ppm, 1000 ppm, and 2000 ppm were synthesised under sintering conditions of 1700 °C (1973.15 K) and -420 kJ/mol. It was found by extracting single crystal grains and cross-analysing these against the bulk mother material using HERFD-XANES and EXAFS ambient condition measurements supported by theoretical calculations that Mn incorporates into UO_2 as Mn^{+2} substituting for U position, with the additional formation of Mn^{+2}O as a secondary phase. Other substitution mechanisms, such as through cluster formation or interstitial inclusion are less likely to occur based on electronic

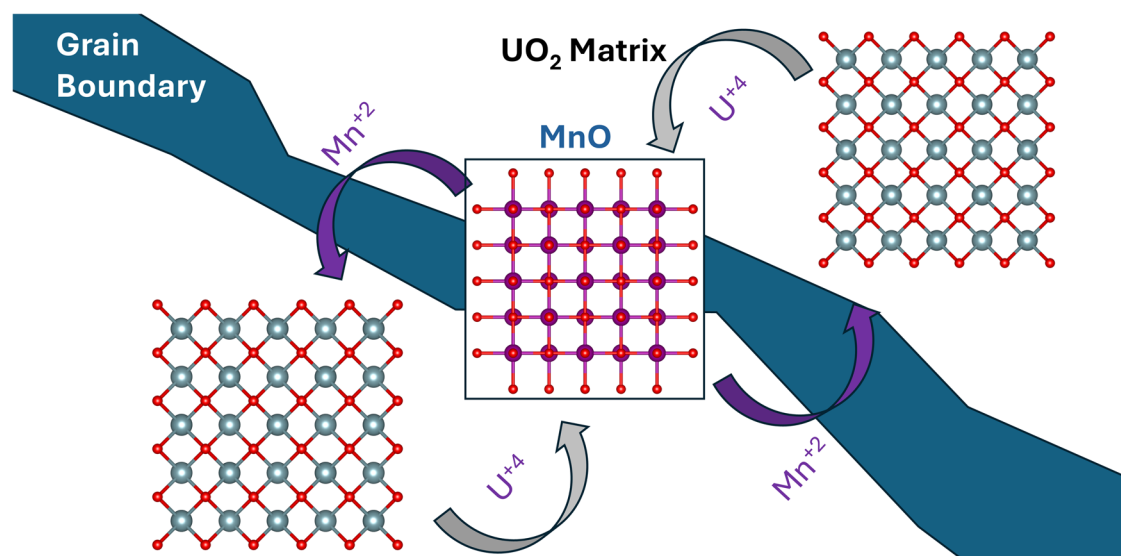


Fig. 7 | Graphical illustration of cation migration and incorporation during material sintering of UO_2 and MnO identified in this study. Graphical illustration of the cation migration that occurs during the high-temperature sintering of Mn-doped UO_2 as determined from S-XRD, HERFD-XANES, and EXAFS measurements of the present investigation. It is argued that the isostructural relationship that

exists between fluorite Mn^{2+}O and UO_2 , both in space group $Fm\bar{3}m$, facilitates mutual incorporation of U and Mn^{2+} cations via solid solution, in which the diversion of U cations from other UO_2 grains to the MnO phase significantly reduces the grain growth capacity in Mn-doped UO_2 . Purple, red and blue spheres respectively represent Mn, U, and O atoms.

structure calculations. By considering the solid-state chemistry of UO_2 , in addition to observations made based on S-XRD, HERFD-XANES and EXAFS measurements the charge balancing for the incorporation of Mn^{2+} into UO_2 is argued to follow an oxygen defect formation mechanism with Mn^{2+} directly substituting for a U position, $(\text{Mn}_x^{2+}\text{U}_{1-x}^{4+})\text{O}_{2-x}$. S-XRD measurements analysed using the Rietveld method suggest relatively similar levels of solubility of Mn within UO_2 as found for Cr-doping under the same conditions, whereas the near consistent rate of lattice contraction supports a like charge balancing mechanism of oxygen defect formation⁵. SEM-EDS measurements performed on ceramic bodies indicated only a crude increase in average grain size compared to pure UO_2 from Mn addition, inferior to Cr-doped UO_2 under similar conditions⁵. Pertinently, it was identified through EXAFS measurements on sintered material that in addition to Mn^{2+} incorporating into the UO_2 lattice matrix, U cations are also incorporated within the MnO secondary phase via solid solution behaviour. This process is considered to be facilitated via the isostructural relationship that exists between fluorite UO_2 and MnO both in space group $Fm\bar{3}m$. It is consequently argued that the inhibited grain growth of Mn-doped UO_2 , despite predicted to be superior to Cr-doped UO_2 in average grain growth¹², arises from the MnO secondary phase parasitically incorporating U cations that should migrate to other UO_2 grains during sintering. Moreover, this investigation has comprehensively determined redox chemistry within Mn-doped UO_2 and critically highlights the need to consider the total solid-state chemistry and interactions of secondary phases during the design and sintering for advanced ceramics in nuclear fuel applications and beyond.

Methods

Synthesis

Mn-doped UO_2 samples were synthesised using a previously developed method for Cr-doped UO_2 ^{5,6} via co-precipitation utilising doped ammonium diuranate (ADU). Stoichiometric amounts of uranyl nitrate ($\text{UO}_2(\text{NO}_3)_2$) and manganese nitrate ($\text{Mn}(\text{NO}_3)_2$) were mixed in solution followed by precipitation using ammonia (NH_3) with a 300% excess applied. The doped ADU mixtures were calcined initially using a box furnace at 800 °C for 5 h prior to reduction to UO_2 at 600 °C via a 4% H_2 -96% Ar atmosphere for a further 5 h. In these steps, the samples were in a powder state. The reduced powders were then compacted into pellets and heated to 1700 °C using a tube furnace for 10 h with a μO_2 of -420 kJ/mol that was

monitored and produced via a 4% H_2 -96% Ar with 1% O_2 -99% Ar gas mixture. Post-synthesis, samples were carefully mechanically divided for specific measurement analysis. Four samples of Mn-doped UO_2 were synthesised using additions of Mn for 0 ppm, 500 ppm, 1000 ppm, and 2000 ppm as Mn elemental.

SEM

The morphology, grain size and average distribution of Mn were determined using a FEI Quanta 200F Environmental scanning electron microscope (SEM) fitted with an energy-dispersive X-ray spectrometer (EDS). Surfaces of parts of the sintered pellets were embedded in resin and carefully polished using diamond pastes (up to 1 μm) and finished with a colloidal Si-suspension. The samples were sputtered with a thin layer of carbon to enhance the electrical conductivity. Backscattered electron (BSE) images were collected at 10 kV to obtain a high-orientation contrast image to identify single grains. The procedure of Podor et al.³⁸ was used for image acquisition, a semi-automatic segmentation of grain boundaries and the determination of grain sizes. EDS spot analyses, as well as EDS elemental mappings, to determine the spatial distribution of Mn, were carried out at 20 kV and a working distance of 10 mm. Single crystal grains were measured neat pre-HERFD-XANES and EXAFS measurements to check crystal purity and particularly the absence of surface Mn oxide impurities and contaminants.

Synchrotron X-ray powder diffraction

Samples were measured as powders using synchrotron X-ray diffraction powder diffraction (S-XRD) measurements under ambient conditions were performed at the BM20 Rossendorf beamline³⁹ (ROBL) at the European Synchrotron Radiation Facility (ESRF), Grenoble, France. Diffraction data were collected on a high-resolution XRD1 machine equipped with a Dectris Eiger CdTe 500k photon counting detector at 23 °C. Synthesised samples were finely ground and packed in glass capillaries of 0.3 mm diameter enclosed in 1 mm Kapton tubes that serve as confinement barriers. The monochromator energy was calibrated against the K-edge X-ray absorption spectrum of a yttrium metal foil using the first inflection point at 17,038 eV which provides an uncertainty of ± 0.3 eV (± 0.000013 Å). The energy was then shifted and set to 16 000 eV and the detector geometry of the experimental setup was calibrated using silver behenate and a LaB_6 NIST standard

reference. The wavelength was subsequently determined to be 0.7749 Å. Experiments were performed in transmission mode at 23 °C and corresponding 2D data were reduced using the PyFAI library adapted for diffractometers mounted on a goniometer arm⁴⁰. Collected diffractograms were analysed using the Rietveld method in the programme GSAS-II^{41,42}. This analysis indicated the formation of single-phase fluorite materials in space group $Fm\bar{3}m$ consistent with the general UO_2 fluorite structure for all examined compositions. Refinement profiles are given in Supplementary Information Note 1 and discussed in further detail in subsequent sections.

Single crystal X-ray diffraction and mechanical separation of single crystal grains

Single crystal grains were mechanically separated from the synthesised material by first breaking the pellets and then cutting them under a microscope. Note, that single crystal grains were separated immediately after synthesis i.e. not subjected to SEM polishing or other chemical treatments. Single crystal X-ray diffraction (SC-XRD) measurements were performed on single crystal grains using an Agilent Oxford diffraction super nova diffractometer with a Mo K α tube at 296 K, equipped with CrysAlisPro software. The unit cell was determined, and background effects were processed by the CrysAlisPro software. The initial structures were refined using SHELXL-2018 within the WinGX (v1.80.05) software⁴³, and the ADDSYM algorithm of the PLATON programme⁴⁴ was used for the checking of possible higher symmetries. Absorption corrections for the raw data were performed using the multiscan method. Samples of appropriate crystal purity i.e. confirmation of the UO_2 fluorite structure and to the limits of resolution free of twinning, contaminant material or incorrect reflections were separated for later analysis. No attempts were made to determine the position of Mn atoms within UO_2 crystals from SC-XRD measurements.

HERFD-XANES spectroscopy

HERFD-XANES spectra were collected at room temperature using an X-ray emission spectrometer equipped with five Ge(333) crystal analysers with a 1 m bending radius, and a silicon drift X-ray detector in a vertical Rowland geometry⁴⁵. For Mn K-edge HERFD-XANES measurement, the spectrometer was tuned to the maximum 5900.3 eV X-ray emission line using the 111 reflections of a Ge analyser at a Bragg angle of 74.8°. For U M_4 -edge HERFD-XANES measurements, the spectrometer was tuned to the maximum $U\ M\beta$ (3d3/2 – 4f5/2, 3337 eV) X-ray emission line using the Si (220) reflection with a Bragg angle of 75°. For U L_3 -edge HERFD-XANES measurements, the spectrometer was tuned to the maximum $U\ L\alpha_1$ (2p3/2 – 3d5/2, 13,614 eV) X-ray emission line using the Si (880) reflection with a Bragg angle of 71.5°. The detected intensity was normalised to the incident flux for both edges. The beam size was estimated to be 30 μ m (vertically) by 1000 μ m (horizontally). Mn-doped UO_2 powder and a single crystal grain extracted from the 2000 ppm Mn addition sample were measured on the Mn K-edge in addition to the Mn standards: $Mn^{+2}Cl_2$, $Mn^{+3}O_3$, Mn (Mn^0) metallic, $Mn^{+3}F_3$, $Mn^{+2}O$ and $Mn^{+4}O_2$. For Mn-doped UO_2 powder and single crystal grains, the former was mounted without a backing matrix and the latter as neat monoliths, both encapsulated in Kapton for radiation protection. A number of single crystals were examined using HERFD-XANES, the final specimen chosen for analysis was the largest one which was deemed to have the most Mn within it and subsequently produced the strongest signal. Mn-doped UO_2 powder was measured with UO_2 on the $U\ M_4$ -edge and $U\ L_3$ -edge.

Electronic structure calculations

FDMNES²⁹ calculations of the Mn K edge XANES were performed considering a cluster of ~100 atoms around the absorber. Within this cluster, the atomic potential was calculated self-consistently. The simulations were performed on the standard MnO structure and on structural models for the incorporation of Mn in the UO_2 structure. The incorporation of the Mn atom was considered in three configurations: as a cluster replacing the U atom and the second nearest neighbours with Mn, as an interstitial atom, and as a single impurity included in the structure substituting a U position.

EXAFS

EXAFS measurements were conducted on an Mn-doped UO_2 powder sample with 2000 ppm Mn addition using high energy resolution fluorescence detection (HERFD) mode and X-ray emission spectrometer as explained above. For the sample, twelve spectra were collected, followed by dead-time correction and energy calibration using EXAFSPAK⁴⁶. Data reduction and Fourier transform (FT) of the EXAFS data over a constant k-range (2.0–8.8 Å⁻¹) with subsequent fitting was conducted using the programme SIXPACK⁴⁷. Theoretical scattering phases and amplitudes were calculated using the ab initio code FEFF8.20⁴⁸. Several theoretical models were used as input for the fitting of the EXAFS data. The models were based on structures for UO_2 and MnO with Mn substitution for the host cation site. The error arising from the EXAFS structural determination is mainly determined by two sources which are (1) model assumptions taken for the calculation of the theoretical EXAFS signals (FEFF calculation) and (2) the intrinsic error of the data, i.e. experimental error like noise or beam fluctuations etc., and the shell fit model. The latter error (2) is reflected by the standard deviations provided for the variable parameter as determined by the statistical shell fit procedure contained in the suit of EXAFSPAK. Both errors lead to a common uncertainty in the determination of radial distances (R) and coordination numbers (CN) of $R \pm 0.02$ Å and $CN \pm 20\%$, respectively⁴⁹.

Data availability

The data that support the findings of this study are available from the corresponding author, upon reasonable request.

Received: 23 July 2024; Accepted: 3 December 2024;

Published online: 19 December 2024

References

1. Degueldre, C., Bertsch, J., Kuri, G. & Martin, M. Nuclear fuel in generation II and III reactors: research issues related to high burn-up. *Energy Environ. Sci.* **4**, 1651–1661 (2011).
2. Arborelius, J. et al. Advanced doped UO_2 pellets in LWR applications. *J. Nucl. Sci. Technol.* **43**, 967–976 (2006).
3. Delafoy, C. & Dewes, P. AREVA NP new UO_2 fuel development and qualification for LWRs applications. In *Top Fuel 1–7* (European Nuclear Society, Salamanca, 2006).
4. Gamble, K. A., Pastore, G., Andersson, D. & D. Cooper, M. W. *Bison Capability and Validation for U_3Si_2 , Cr_2O_3 -Doped UO_2 , Fecral, and Cr-Coated Zircaloy Atf Concepts* (Idaho National Lab. (INL), Idaho Falls, 2020).
5. Murphy, G. L. et al. Deconvoluting Cr states in Cr-doped UO_2 nuclear fuels via bulk and single crystal spectroscopic studies. *Nat. Commun.* **14**, 2455 (2023).
6. Kegler, P. et al. Chromium doped UO_2 -based ceramics: synthesis and characterization of model materials for modern nuclear fuels. *Materials* **14**, 6160–6178 (2021).
7. Devillaire, A. et al. Characterisation of 3000 ppm Cr_2O_3 doped UO_2 and its precipitates. *J. Raman Spectrosc.* **54**, 1–7 (2023).
8. Riglet-Martial, C. et al. Thermodynamics of chromium in UO_2 fuel: a solubility model. *J. Nucl. Mater.* **447**, 63–72 (2014).
9. Leenaers, A., de Tollenaere, L., Delafoy, C. & Van den Berghe, S. On the solubility of chromium sesquioxide in uranium dioxide fuel. *J. Nucl. Mater.* **317**, 62–68 (2003).
10. Killeen, J. Fission gas release and swelling in UO_2 doped with Cr_2O_3 . *J. Nucl. Mater.* **88**, 177–184 (1980).
11. Cooper, M. W. D., Andersson, A. D. R. & Stanek, C. R. *Mn-Doped Oxide Nuclear Fuel*. (Los Alamos National Lab. (LANL), Los Alamos, 2020).
12. Cooper, M. W. D., Stanek, C. R. & Andersson, D. A. The role of dopant charge state on defect chemistry and grain growth of doped UO_2 . *Acta Mater.* **150**, 403–413 (2018).

13. Finkeldei, S. et al. *Synthesis and Characterization of UO₂ Feedstocks Containing Controlled Dopants* (Oak Ridge National Lab. (ORNL), Oak Ridge, 2019).
14. Fujino, T. et al. Post-irradiation examination of high burnup Mg doped UO₂ in comparison with undoped UO₂, Mg–Nb doped UO₂ and Ti doped UO₂. *J. Nucl. Mater.* **297**, 176–205 (2001).
15. Greenquist, I., Tonks, M., Cooper, M., Andersson, D. & Zhang, Y. Grand potential sintering simulations of doped UO₂ accident-tolerant fuel concepts. *J. Nucl. Mater.* **532**, 152052 (2020).
16. Zhong, Y. et al. Densification kinetics and sintering behavior of UO₂ and 0.5 wt.% MnO-doped UO₂. *J. Am. Ceram. Soc.* **106**, 5723–5734 (2023).
17. Smith, H. et al. Fabrication, defect chemistry and microstructure of Mn-doped UO₂. *Sci. Rep.* **14**, 1656 (2024).
18. Kang, K. W. et al. Effects of MnO–Al₂O₃ on the grain growth and high-temperature deformation strain of UO₂ fuel pellets. *J. Nucl. Sci. Technol.* **47**, 304–307 (2010).
19. Middleburgh, S. C. et al. Enrichment of chromium at grain boundaries in chromia doped UO₂. *J. Nucl. Mater.* **575**, 154250–154254 (2023).
20. Toker, N., Darken, L. & Muan, A. Equilibrium phase relations and thermodynamics of the Cr–O system in the temperature range of 1500 °C to 1825 °C. *C. Metall. Trans. B* **22**, 225–232 (1991).
21. Kang, Y.-B. & Jung, I.-H. Thermodynamic modeling of oxide phases in the Mn–O system. *Metall. Mater. Trans. E* **3**, 156–170 (2016).
22. Bourgeois, L., Dehaut, P., Lemaignan, C. & Hammou, A. Factors governing microstructure development Of Cr₂O₃-doped UO₂ during sintering. *J. Nucl. Mater.* **297**, 313–326 (2001).
23. Gonzalez-Julian, J. Processing of MAX phases: from synthesis to applications. *J. Am. Ceram. Soc.* **104**, 659–690 (2021).
24. Lee, J. H., Hong, J. K., Jang, D. H., Sun, Y. K. & Oh, S. M. Degradation mechanisms in doped spinels of LiM_{0.05}Mn_{1.95}O₄ (M = Li, B, Al, Co, and Ni) for Li secondary batteries. *J. Power Sources* **89**, 7–14 (2000).
25. Murphy, G. L. et al. The lattice contraction of UO₂ from Cr doping as determined via high resolution synchrotron X-ray powder diffraction. *J. Nucl. Mater.* **595**, 155046 (2024).
26. Peres, V. et al. High temperature chromium volatilization from Cr₂O₃ powder and Cr₂O₃-doped UO₂ pellets in reducing atmospheres. *J. Nucl. Mater.* **423**, 93–101 (2012).
27. Lan, F.-J. et al. Study on manganese volatilization behavior of Fe–Mn–C–Al twinning-induced plasticity steel. *High. Temp. Mater. Process.* **40**, 461–470 (2021).
28. Stenzel, A., Fähsing, D., Schütze, M. & Galetz, M. C. Volatilization kinetics of chromium oxide, manganese oxide, and manganese chromium spinel at high temperatures in environments containing water vapor. *Mater. Corros.* **70**, 1426–1438 (2019).
29. Joly, Y. et al. Self-consistency, spin-orbit and other advances in the FDMNES code to simulate XANES and RXD experiments. in *Journal of Physics: Conference Series* 012007, Vol. 190 (IOP Publishing, 2009).
30. Shannon, R. Revised effective ionic radii and systematic studies of interatomic distances in halides and chalcogenides. *Acta Crystallogr. Sect. A* **32**, 751–767 (1976).
31. Kleykamp, H. Phase equilibria in the UO₂-austenitic steel system up to 3000 °C. *J. Nucl. Mater.* **247**, 103–107 (1997).
32. Ohmichi, T., Fukushima, S., Maeda, A. & Watanabe, H. On the relation between lattice parameter and O/M ratio for uranium dioxide-trivalent rare earth oxide solid solution. *J. Nucl. Mater.* **102**, 40–46 (1981).
33. Hillert, M. On the theory of normal and abnormal grain growth. *Acta Metall.* **13**, 227–238 (1965).
34. Sasaki, S., Fujino, K. & Takéuchi, Y. X-ray determination of electron-density distributions in oxides, MgO, MnO, CoO, and NiO, and atomic scattering factors of their constituent atoms. *Proc. Jpn. Acad. Ser. B* **55**, 43–48 (1979).
35. Zhong, Y. et al. Densification and grain growth of UO₂ and MnO–UO₂ during pressureless sintering. *J. Eur. Ceram. Soc.* **44**, 2383–2394 (2024).
36. Mathis, T. S. et al. Modified MAX phase synthesis for environmentally stable and highly conductive Ti₃C₂ MXene. *ACS nano* **15**, 6420–6429 (2021).
37. Palanki, B. Some factors affecting densification and grain growth in the sintering of uranium dioxide—a brief review. *J. Nucl. Mater.* **550**, 152918 (2021).
38. Podor, R. et al. Evaluation and application of a new scintillator-based heat-resistant back-scattered electron detector during heat treatment in the scanning electron microscope. *J. Microsc.* **282**, 45–59 (2021).
39. Scheinost, A. C. et al. ROBL-II at Esrf: a synchrotron toolbox for actinide research. *J. Synchrotron Radiat.* **28**, 333–349 (2021).
40. Kieffer, J., Valls, V., Blanc, N. & Hennig, C. New tools for calibrating diffraction setups. *J. Synchrotron Radiat.* **27**, 558–566 (2020).
41. Larson, A. C. & Von Dreele, R. B. Gsas. *Report IAU*, 86–748 (1994).
42. Toby, B. H. EXPGUI, a graphical user interface for GSAS. *J. Appl. Crystallogr.* **34**, 210–213 (2001).
43. Sheldrick, G. A short history of SHELX. *Acta Crystallogr. Sect. A* **64**, 112–122 (2008).
44. Spek, A. Single-crystal structure validation with the program PLATON. *J. Appl. Crystallogr.* **36**, 7–13 (2003).
45. Kvashnina, K. O. & Scheinost, A. C. A Johann-type X-ray emission spectrometer at the Rossendorf beamline. *J. Synchrotron Radiat.* **23**, 836–841 (2016).
46. EXAFSPAK: A Suite Of Computer Programs For Analysis Of X-Ray Absorption Spectra (Stanford Synchrotron Radiation Laboratory, Stanford, 1995).
47. Ressler, T. Winxas: a program for X-ray absorption spectroscopy data analysis under Ms-windows. *J. Synchrotron Radiat.* **5**, 118–122 (1998).
48. Ankudinov, A. L., Ravel, B., Rehr, J. & Conradson, S. Real-space multiple-scattering calculation and interpretation of X-ray-absorption near-edge structure. *Phys. Rev. B* **58**, 7565–7576 (1998).
49. Li, G. G., Bridges, F. & Booth, C. H. X-ray-absorption fine-structure standards: a comparison of experiment and theory. *Phys. Rev. B* **52**, 6332–6348 (1995).
50. Desgranges, L., Baldinozzi, G., Rousseau, G., Nièpce, J.-C. & Calvarin, G. Neutron diffraction study of the in situ oxidation of UO₂. *Inorg. Chem.* **48**, 7585–7592 (2009).

Acknowledgements

The authors are grateful for the funding and support from the German Federal Ministry of Education and Research (BMBF), project no. 02NUK060, which enabled this research. The authors are also thankful for the Ge111 crystals supplied by the ID26 beamline of the ESRF for the Mn K-edge measurements.

Author contributions

The project was conceived and developed by Gabriel L. Murphy. The research methodology, experimental planning, and formal analysis were conducted by Gabriel L. Murphy. The materials were synthesised by Gabriel L. Murphy, Andrey Bukaemskiy, and Maximilian Henkes. Single crystal grains were extracted and characterised with single crystal X-ray diffraction by Gabriel L. Murphy. Synchrotron powder diffraction measurements and analysis were performed by Gabriel L. Murphy, Jessica Lessing, Julien Marquardt Volodymyr Svitlyk and Christoph Hennig. Scanning electron microscopy measurements and analysis were made by Robert Thümmeler and Martina Klinkenberger. X-ray absorption spectroscopy measurements were performed by Gabriel L. Murphy, Nina Huittinen, Julien Marquardt, Elena Bazarkina, and Kristina Kvashnina. Electronic structure calculations were performed by Clara L. Silva, Lucia Amidani, and Kristina Kvashnina. Extended X-ray absorption fine structure measurements and analysis were performed by Nina Huittinen and Andre Rossberg. Manuscript writing, review and editing were performed by Gabriel L. Murphy with input from all authors.

Funding

Open Access funding enabled and organized by Projekt DEAL.

Competing interests

The authors declare no competing interests.

Additional information

Supplementary information The online version contains supplementary material available at

<https://doi.org/10.1038/s43246-024-00714-x>.

Correspondence and requests for materials should be addressed to Gabriel L. Murphy.

Peer review information *Communications materials* thanks Dario Manara and the other, anonymous, reviewer(s) for their contribution to the peer review of this work. Primary handling editor: John Plummer. A peer review file is available.

Reprints and permissions information is available at <http://www.nature.com/reprints>

Publisher's note Springer Nature remains neutral with regard to jurisdictional claims in published maps and institutional affiliations.

Open Access This article is licensed under a Creative Commons Attribution 4.0 International License, which permits use, sharing, adaptation, distribution and reproduction in any medium or format, as long as you give appropriate credit to the original author(s) and the source, provide a link to the Creative Commons licence, and indicate if changes were made. The images or other third party material in this article are included in the article's Creative Commons licence, unless indicated otherwise in a credit line to the material. If material is not included in the article's Creative Commons licence and your intended use is not permitted by statutory regulation or exceeds the permitted use, you will need to obtain permission directly from the copyright holder. To view a copy of this licence, visit <http://creativecommons.org/licenses/by/4.0/>.

© The Author(s) 2024